metals

MDPI

Article

Application of Vacuum Techniques in Shell Moulds Produced by Additive Manufacturing

P. Rodríguez-González *, P. E. Robles Valero, A. I. Fernández-Abia, M. A. Castro-Sastre and J. Barreiro García

Department of Mechanical, Informatics and Aerospace Engineering, University of León, Campus de Vegazana, 24071 León, Spain; probv@unileon.es (P.E.R.V.); aifera@unileon.es (A.I.F.-A.); macass@unileon.es (M.A.C.-S.); jbarg@unileon.es (J.B.G.)

* Correspondence: prodrg@unileon.es; Tel.: +34-98-729-1000 (ext. 5270)

Received: 10 July 2020; Accepted: 9 August 2020; Published: 12 August 2020

Abstract: This research shows the feasibility of the additive manufacturing technique (AM), Binder Jetting (BJ), for the production of shell moulds, which are filled by vacuum suction in the field of aluminium parts production. In addition, this study compares the gravity pouring technique and highlights the advantages of using vacuum techniques in AM moulds. A numerical simulation was carried out to study the behaviour of the liquid metal inside the moulds and the cooling rate of parts was analysed. The results show that in the gravity-pouring mould, the velocity in the gate causes moderate turbulence with small waves. However, vacuum suction keeps the velocity constant by eliminating waves and the filling process is homogeneous. Regarding dimensional accuracy, the staircase effect on the surface of the 3D moulds was the most critical aspect. The vacuum provides very homogeneous values of roughness across the entire surface of the part. Similarly, 3D scanning of castings revealed more accurate dimensions thanks to the help of vacuum forces. Finally, the microstructure of the cross section of the moulded parts shows that the porosity decreases with the vacuum filled. In both cases, the origin of the pores corresponds to gas entrapment and shrinkage during the filling process, the binder vaporization and nucleation points creation, leading to pores by shrinkage, gas entrapment or a mixture of both. This is the first study that uses vacuum filling techniques in moulds created by BJ, demonstrating the feasibility and advantages of AM using vacuum techniques, as an alternative to traditional casting.

Keywords: additive manufacturing; binder jetting; aluminium casting; vacuum assisted; calcium sulphate

1. Introduction

Additive manufacturing technology (AM) is based on the manufacture of parts or products by adding layers of material. It was originally developed to produce rapid prototypes. Today, this technology has many applications in different industrial sectors [1].

One of the AM techniques that is receiving more attention lately is the binder jetting (BJ) technique [2]. This technique is based on joining powder by means of a binder [3]. The process starts by spreading a layer of powder on a platform using a roller. Then, micro-droplets of a liquid binder are selectively injected through a print-head. This creates a two-dimensional layer where the powders that receive the binder bond with each other. The platform then descends a distance equivalent to the thickness of the layer and the process is repeated according to the slicing software. Finally, a three-dimensional part called the "green part" is obtained, which is usually post-treated to improve the final properties [4,5].

The applications of this technique are present in diverse sectors from aeronautics [6] to biomedical [7–9]. However, much effort is being made to use the BJ technique in the foundry

industry, as it reduces time and cost [10]. Chen et al. [11] reviewed the techniques used in 3D printing for ceramic materials and concluded that the BJ technique is the most suitable for manufacturing moulds or cores. Although metal casting dates back to ancient times, the evolution of materials and technology drives the further development of knowledge about this industry [12].

Current market requirements make the traditional foundry industry uncompetitive when low quantities are requested [13]. However, AM has proven to be useful for making small or single series castings as well as for validating prototypes that are then manufactured on a mass scale. The BJ technique offers several advantages, such as design freedom, minimum material waste, lower tooling costs and improved supply chain efficiency [14]. Almaghariz et al. [15] identified the breakeven point where 3D printing is cost-effective for castings, considering the level of complexity. They demonstrated that AM fast casting technology is very efficient for manufacturing up to 45 units for simple parts and up to 1000 units for extremely complex parts. After these amounts, traditional casting methods start to become more cost-effective.

Mould design has few limitations when using the BJ technique. Shangguan et al. [16] and Kang et al. [17] manufactured casting moulds created by 3D printing reinforced with rib or lattice structures. This new concept of design improved the heat transfer and improved the control of cooling. In addition, the new designs made lighter moulds. They concluded that rapid and uniform cooling improves production efficiency and reduces deformation, residual stress and casting defects. Deng et al. [18] developed 3D printed moulds with internal hollow structures to control local cooling in the castings. They observed that forcing air through the internal ducts around the part cavity improved its cooling. On the other hand, the internal hollows in the feed system functioned as insulators, which allowed the metal to take longer to solidify, improving the filling.

Sama et al. [19] developed unconventional design rules in the filling system to reduce surface turbulence, oxide films and air entrapment, improving the performance of the foundry. In another study, the same authors [20] investigated new designs of sprues for moulds manufactured by the BJ technique, concluding that the use of a conical helical sprue reduces the turbulence of the metal and reduces the volume of casting defects, improving the resistance to bending of the obtained parts.

Wang et al. [21] redesign a casting part using topological optimization. The new casting part improved the safety factor by 30% and reduced its weight by 50% compared to the original casting. Although this study did not consider the impact of other aspects of castings such as surface roughness and errors due to the solidification process.

The inherent design freedom of the BJ technique and its use for small series does not allow the application of a trial and error method for optimizing geometries, because it would not be economically viable. This has encouraged the need to use numerical simulation software to evaluate the effectiveness of the geometries, and to predict the flow behaviour during the filling and solidification process inside the mould.

Yang et al. [22] developed a mathematical model using the Navier-Stokes equation for the pouring and solidification stages; they validated the simulation results, analysing the casting defects. Behera et al. [23] generated a numerical simulation model to analyse the thermal stresses generated in a casting mould. The data results from the simulation, provided an accurate prediction of defects in the mould and the casting. Sun et al. [24] simulated a low-pressure casting process to analyse the origin of the defects found in the castings, confirming that they are due to gas entrainment.

Although the BJ-technique has been successfully proved in the foundry industry, it still presents challenges to overcome. The composition, size and shape of the powder are very important parameters to achieve high quality parts. Zhao et al. [25] observed that the particle size of the powder directly affects roughness of castings, concluding that if the size of the mould particles is reduced, the average roughness decreases and, therefore, the roughness of the casting is reduced. In addition, Du et al. [26] observed that by increasing the number of fine particles in the powder, the surface roughness of the cast iron decreases as fine particles settle between larger particles, reducing the roughness of the mould.

Another very important aspect is powder compaction. There is a general lack of densification during the printing. The low density and the porosity created during the manufacturing is transferred to the green part and the final properties of the moulds [27]. Hodder et al. [28] analysed the mould quality created by AM using local sand as raw material. They concluded that traditional foundry sand can be used inside a 3D printer, but the use of this type of powder generates less optimal moulds. The analysis revealed that dimensional quality and roughness were worse for this type of technique compared to traditional techniques, due to the low powder compaction and the bleeding effect.

Another major issue is adhesive agents. Trombetta et al. [29] have defined a print parameter called "binder level" as the percentage of the space without powder that is filled with binder. It is related to the saturation level and does not depend on the apparent density of the layer. This way, the optimum binder level can be obtained.

The mechanical properties and roughness of the part depend on the quantity of binder. An insufficient quantity of binder cannot join the powder strongly and the printing process will fail. On the other hand, an excessive quantity of binder can cause gross printed lines and/or bleeding effect. This phenomenon deteriorates dimensional accuracy [30].

Bleeding effect is defined as the undesirable migration of the binder on a particle scale outside the intended geometry. Bleeding effect can be controlled by improving binder evaporation, however this can leave pockets in the structure, reducing the mechanical strength. Although the strength of the parts is expected to improve when increasing saturation, this is not always true [31]. Therefore, the amount of binder must be handled carefully when a casting mould is manufactured. Excessive binder may create gases during the casting process that cause erosion in the mould structure or defects in the castings. Snelling et al. [32] manufactured binder injection moulds, using ZCast® and ExOne silica powder. They concluded that moulds created with ZCast® material produced lower quality castings due to gas defects associated with a high level of saturation.

Binders such as furan are predominantly used in foundry applications, but they generate toxic and carcinogenic gases, harmful to operators and the environment. These aspects lead to important limitations, therefore it is necessary to investigate alternative materials for safer and environmentally friendly casting [33]. Rodriguez et al. [34] demonstrated that the manufacture of moulds using the BJ technique with alternative materials can be an option for the use of furan resins.

Vacuum Suction Casting (VSC) is commonly used to avoid gas entrapment defects caused by the binder evaporation or the mould calcination. This process consists of generating a negative pressure in the mould, capable of extracting or compressing the gas generated during the casting process.

Molten metal must remain in a liquid state long enough for the vacuum effect to act. In addition, the pressure difference operates as an injector that forces the metal into the mould, reducing the filling time and avoiding turbulences. Compared to conventional casting technique, vacuum suction casting can obtain high quality parts and improve the qualification rate.

One of the mainly used alloys in the casting industry are Al-Si alloys due to their good mechanical properties, low density and high corrosion resistance. In addition, the casting capacity of these alloys allows the manufacture of components with complex geometries. However, traditional casting techniques have metallurgical properties with imperfections, due to either gas entrapment, shrinkage or the casting technique itself. Some authors have studied the application of vacuum techniques to increase the properties of aluminium alloys. Szklarz et al. [35] investigated the effect of vacuum on the microstructure and the electrochemical response for a specimen as-cast 2017 aluminium alloy. They concluded that by applying vacuum techniques, a more homogeneous microstructure and better corrosion resistance in chlorides is obtained. Liu et al. [36] studied the filling behaviour for an A356 alloy as a function of the depressurization rate, and observed that a high depressurization rate caused the speed at the gate to remain unchanged.

Cao et al. [37] investigated the effect of the T6 treatment on the microstructure and the mechanical properties of a die-cast Al-Si-Cu alloy with three degrees of vacuum. The same authors [38] also studied the influence of different degrees of vacuum on AlSi9Cu3 alloy castings parts created by

vacuum-assisted high-pressure injection (HPDC). In both studies, they concluded that as absolute pressure decreases, average porosity and pore sizes are reduced and tensile strength and elongation are significantly improved.

Vacuum suction is a technique commonly used in the industry to improve the properties of cast parts. The purpose of this research is to demonstrate the improvement of properties in moulds manufactured by AM, being the first known study in which the vacuum suction technique is applied to moulds manufactured by BJ. To demonstrate the improvements of the vacuum suction technique, two moulds were manufactured using the BJ technique and filled using the different techniques (gravity and vacuum assisted pouring). The casting parts were compared and it was possible to quantify the improvement that the vacuum offers to the casting parts and the feasibility of using vacuum processes in the BJ technique.

2. Materials and Methods

2.1. Mould Design

A part was designed specifically to compare the quality of both casting techniques (gravity and vacuum). The design has a high volume/area ratio that maximizes the defects due to shrinkage and internal porosity. An ellipsoidal central geometry was chosen with two cylindrical parts at both ends (Figure 1a). On the other hand, the curved surfaces of the part facilitate the evaluation of the characteristic staircase effect of AM technology. The theoretical weight and volume of the Computer Aided Design (CAD) part is 0.6 kg and 223.4 cm^3, respectively. The casting material was a cast alloy from the AlSi series. The chemical composition is shown in Table 1.

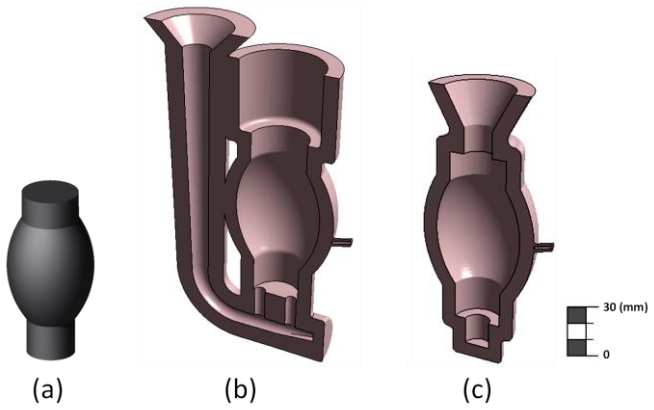

Figure 1. (**a**) Nominal design of the casting part. (**b**) Cross section of the gravity-pouring mould. (**c**) Cross section of the vacuum-assisted mould.

Table 1. Chemical composition of the AlSi alloy (wt.%).

Designation	Al	Si	Fe	Cu	Mn	Mg	Zn	Ni	Ti	Pb	Sn	Kg
EN-AC 4600	Bal.	9.25	1.10	2.08	0.22	0.09	0.92	0.06	0.08	0.05	0.01	5.105

The filling system for both moulds was designed and calculated considering the limitations and advantages of the BJ technique. The moulds are a 10 mm thickness shell, sufficient to withstand the pressure of the molten metal [18]. For the gravity-pouring mould, Figure 1b, the filling system was composed of a sprue with a decreasing circular section describing an arc large enough to prevent cavitation and turbulence during the filling process. This sprue was connected to two vertical gates [39] leading to the cavity of the casting part. Finally, an open top riser was placed to prevent shrinkage defects due to solidification. In addition, it allows a reduction in the metallostatic pressure during the filling process [34]. With this design, the total volume of the 3D Printing (3DP) mould for gravity-pouring is 449 cm^3, the metal yield is 49.75%, and the weight of the mould is 0.55 kg.

For the vacuum-assisted mould, Figure 1c, the filling system consists of a conical cup connected directly to the gate. The gate has a cylindrical geometry with a calculated diameter to control the maximum velocity at the entry of the cavity. In addition, the suction force avoids the turbulent flow during the filling process. Finally, a small overflow was placed at the bottom of the mould to prevent the damage due to the molten metal initial jet. With this design, the total volume of the vacuum-assisted mould is 249.8 cm^3, the metal yield is 89.43% and the mould weight is 0.31 kg. A slot was designed in both moulds to place a thermocouple to measure the temperature gradient during the pouring and solidification process. Both moulds were calculated based on the Campbell design rules [40] and were subsequently optimized using the simulation software.

2.2. Simulation

AnyCasting software (AnyCasting CO., LTD, Seoul, Korea) was used to simulate and optimize the filling system for both pouring techniques.

The basic equations to simulate free surface liquid flow were: (i) the complete Navier-Stokes equation, (ii) the continuity equation and (iii) the Volume Fluid method (VoF). For the convergence of the simulation, the Successive Over-Relaxation (SOR) iteration method was used. In addition, to discretize and solve these equations, the AnyCasting software automatically generated a structured tetrahedral mesh of 10,500,000 cells. This number of cells allowed a good adaptation of the mesh to the geometry and it was a sufficient number to represent effectively the flow behaviour inside the moulds. The highest density of cells was accumulated in the places where major changes in the geometry occurred in order to capture in more detail the changes in the flow variables. The initial parameters shown in Table 2 were introduced as boundary conditions to obtain reliable simulation results. The Heat Transfer Coefficient (HTC) between the casting and the mould was chosen as a linear function based on the properties of the mould. These parameters were automatically taken from the database provided by the software. HTC were compared to other studies [41–43] and the results were very similar to the values offered by the software. In this way, it was possible to predict the behaviour of the liquid metal and the turbulence created inside the moulds during the filling process. The two optimized models are shown in Figure 2.

Table 2. Properties of the $AlSi_9Cu_3(Fe)$ aluminium alloy.

Liquidus Temperature (°C)	Solid Temperature (°C)	Density (kg/m^3)	Thermal Conductivity (W/m/k)	Solidification Shrinkage (%)
595	540	2710	96.2	7.14

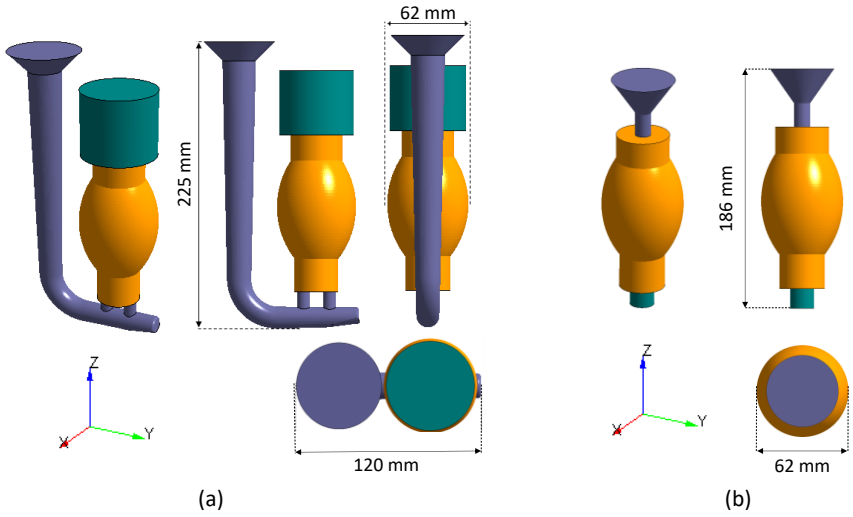

Figure 2. (**a**) 3D model for binder jetting (BJ) gravity-pouring casting system. (**b**) 3D model for BJ vacuum-assisted casting system.

2.3. Binder Jetting Manufactured Moulds

A ProJet CJP 660 Pro (3DSystems, Rock Hill, SC, USA) machine was used to manufacture the moulds. The ceramic material used as core was Visijet PXL. The powder is made up of a mixture of calcium sulfate, dehydrate, hemihydrate and anhydrous phases. In addition, it has some impurities or additives such as aluminium, sodium, magnesium, potassium, silicon [33]. The distribution of powder particles is D90 = 70.12 µm and the bulk particle density is 0.912 g/cm^3 [44]. In addition, the binder used was PXL, a liquid composed of 99% water and 1% of 2-pyrrolidone (C_4H_7NO).

The moulds were placed in the same zone on the machine table, as shown in Figure 3. This zone was chosen because it is the one with the highest powder compaction, as indicated by the manufacturer [45,46]. In addition, the moulds were placed in a horizontal position and in the same direction, to optimize the manufacturing time. The manufacturing parameters used are shown in Table 3.

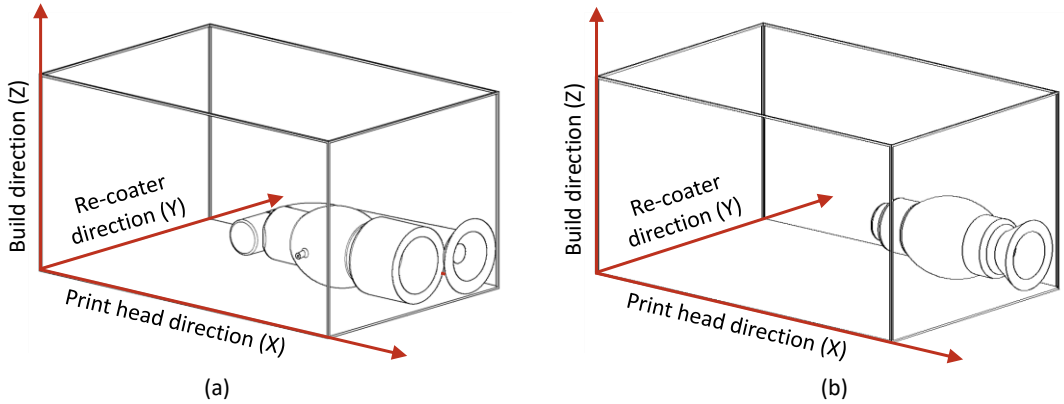

Figure 3. Positioning of the moulds on the machine table related to the axes of the AM ProJet 660Pro machine. (**a**) Gravity-pouring mould. (**b**) Vacuum-assisted mould.

Table 3. Principal parameters of printing.

Printing Parameters	Layer Thickness (µm)	Binder/Volume Ratio of Core *	Binder/Volume Ratio of Shell *	Bleed Compensation X; Y, Z (µm)
Value	102	0.12	0.24	9.1; 7.1; 7.6

* Saturation level at 100%.

Once the manufacturing process was completed, the moulds were extracted from the machine and the unbound powder was removed with a brush and pressurized air. Finally, the moulds received a 2-h heat treatment at 250 °C in a JP Selecta 2001255 (JP Selecta, Barcelona, Spain) furnace to remove the moisture and volatile elements. This process improved the permeability and mechanical strength of the moulds.

2.4. Pouring and Solidification

The casting process started with melting of the aluminium alloy in an AGATRONIC R induction furnace (Argenta, Kielce, Poland). The pouring temperature was 750 ± 5 °C. The holding time was 2 min. The temperature sensor that controls the furnace is housed inside the crucible, therefore the temperature that the sensor reads is the real temperature of the metal liquid. The casting had a small volume and the handling and pouring time was very short, therefore the temperature of the metal liquid during the pouring did not vary significantly. For the gravity-pouring mould it was necessary to rest the mould on a sand base to prevent movement during the casting. In the case of the vacuum-assisted mould, it was placed in the vacuum chamber at the bottom of the furnace. The vacuum system consisted of a GRIÑO ROTAMIK VS 21 EW (GRIÑO ROTAMIK, Rubí, Spain). A vacuum

pump with a flow rate of 24 m^3/h and a maximum vacuum pressure of 0.5 mbar in absolute pressure was used. For the successful performance of the operation, 150 ± 1 mbar of vacuum in absolute scale were applied. The thermocouple K-type connected to EasyLog USB (LASCAR electronics, whiteparish, UK) was placed in the mould housing to measure its temperature during the pouring and solidification process. The process used is shown in Figure 4.

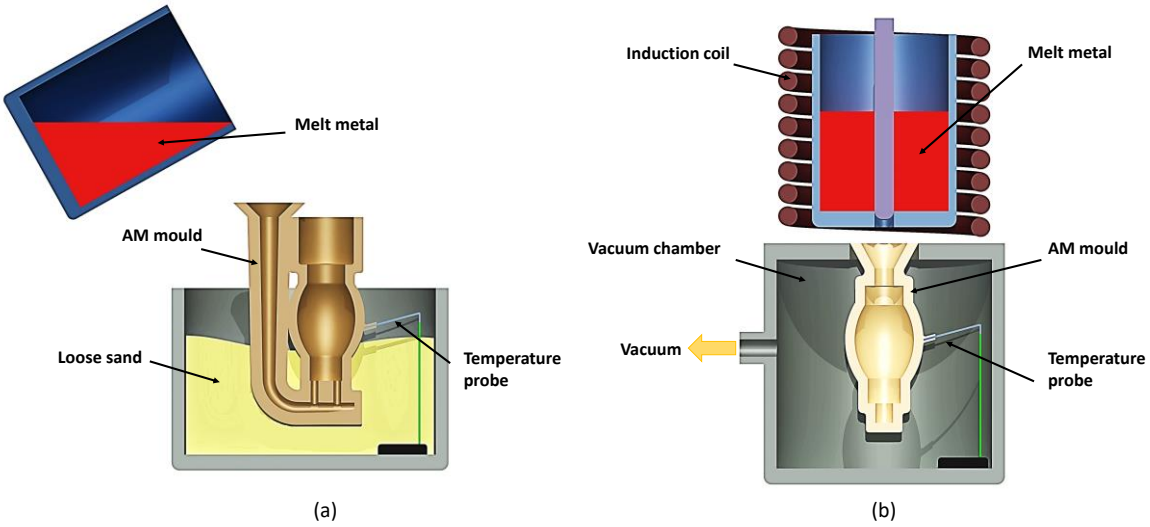

Figure 4. Diagram of the casting process: (**a**) gravity-pouring technique, (**b**) vacuum-assisted technique.

Once the moulds' temperature reached 50 ± 5 °C, the parts were extracted to start the analysis stage. Figure 5 shows the castings (Figure 5a) and final parts (Figure 5b). Three features were selected to compare the castings: surface quality, dimensional quality and porosity.

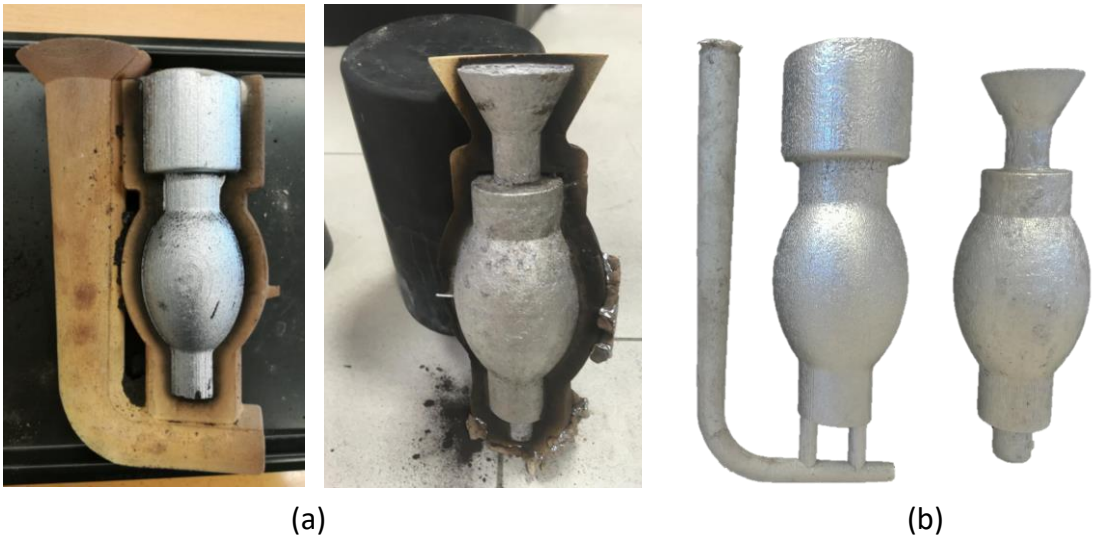

Figure 5. (**a**) Extraction process, (**b**) casting parts.

2.5. Surface Roughness Analysis

The surface quality of the parts was obtained using a Mitutoyo Surftest SJ-500 profilometer (Mitutoyo, Kawasaki-shi, Japan). The cutting length was 2.5 mm and the evaluation length 12.5 mm, according to ISO 4288: 1996 [47]. The measurements were taken in three areas of the part, designated as Zone I, II, and III. In Zones I and III, the measurements were made in two directions: (i) in the direction of the print-head (X direction) and (ii) in the direction of the movement of the re-coater

(Y direction). Zones and directions are shown in Figure 6. The measurements made in the Y direction registered surface irregularities due to the staircase effect characteristic of the 3DP technique. In Zone II, only measurements in the Y direction were made.

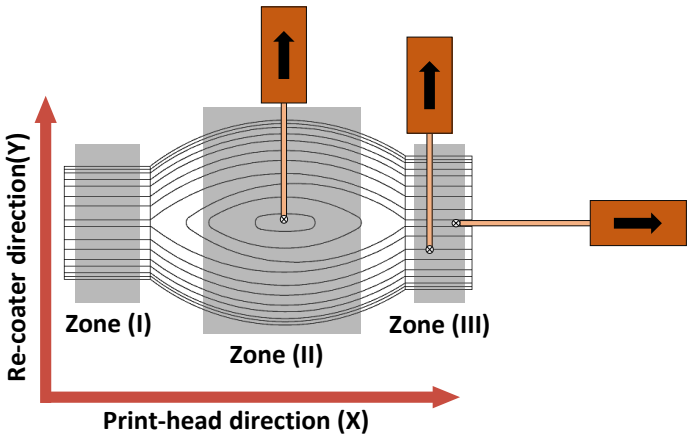

Figure 6. Zones and directions for measuring the roughness of castings.

2.6. Quality Dimensional Analysis

A Breuckmann Smart SCAN3D-HE (Breuckmann, Heiligenhaus, Germany) structured light scanner with a working field of 125 mm and an accuracy of 5 µm was used to analyse the geometrical and dimensional quality of the moulds and parts. The obtained point-clouds were processed by Geomagic Control X software (3D Systems, Rock Hill, SC, USA) for comparing to nominal CAD by Best Fit alignment. The average number of points in each scan was 45,000 points. The average and standard deviations of the total number of points from the CAD was obtained. The tolerance range used was 0.05 mm, divided into upper and lower deviation and all calculated along the maximum deviation, set as 1 to −1 mm. In addition, to observe the differences between the different states, the average deviation of the upper and lower deviation was compared with the percentage of total points in each type of deviation.

The analysis of the dimensional quality was divided into three stages: (i) the moulds were scanned as built. This allowed the analysis of errors induced by the machine and the manufacturing process itself (bleeding effect); (ii) the moulds were scanned after the heat treatment. In this way, the error produced by the elimination of volatiles and the microstructural change suffered during the process was quantified, and (iii) the cast parts were scanned to observe the errors introduced by the casting process (shrinkage). Therefore, the dimensional deviation was the sum of the errors produced by the mould manufacture, the heat treatment and the casting process.

2.7. Porosity Analysis

The volumetric porosity was evaluated on the castings. The control Zones (I, II and III) were sectioned and the hydrostatic weighing method was used [38]. A CB-Complet electronic balance (Cobos Precisión, Barcelona, Spain) with an accuracy of 0.001 g was used to weight the parts.

To analyse the internal porosity and obtain a high resolution of the pores, specimens were extracted in each part at the central and external area of each Zone (I, II and III). The specimens were polished according to standard [48]. A total of 50 images were taken from each specimen, with a Tecmicro metallographic microscope (OLYMPUS BHM, Barcelona, Spain). Finally, the images were evaluated with ImageJ 2016-0205 software (National Institutes of Health, Bethesda, MD, USA). This tool allowed the brightness and contrast of the images to be stabilized, isolating the contour of the holes by applying a threshold filter. In this way, the number of pores, the maximum and minimum Feret diameter (the longest and shortest distance between two points along the selection boundary, respectively) and the roundness of the pores in each region were obtained.

3. Results

3.1. Results of Simulation

The results of the simulation made it possible to know the velocity profile, to avoid a high turbulent flow of the liquid metal during the filling process. Campbell [40] defined the maximum filling speed as 0.5 m/s; increasing this speed value can lead to gas entrainment and oxide films. The colour map in Figure 7 shows the velocity profile of both moulds during the filling process. The vacuum-assisted technique has a more controlled filling, avoiding the possible defects of gas entrapment, inclusions or oxides.

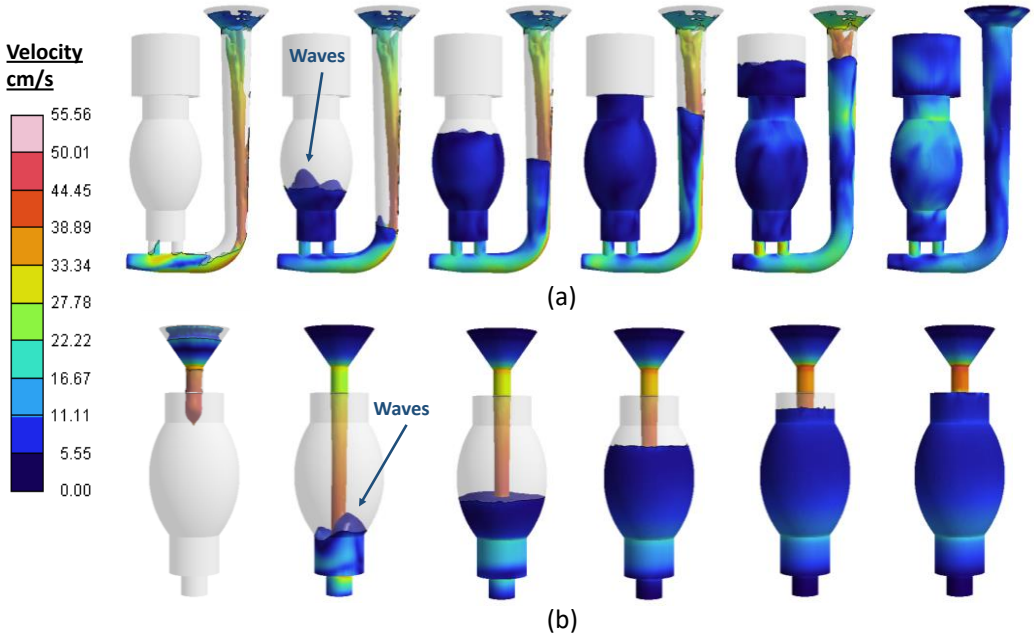

Figure 7. (**a**) Velocity profile for BJ gravity-pouring, (**b**) velocity profile for BJ vacuum-assisted oxide films.

The flow behaviour of the liquid metal inside the gravity-pouring mould was progressive (Figure 7a), with moderate turbulence and a relatively homogeneous velocity profile. Although the filling velocity remained at values very close to 0.5 m/s at some points, this velocity was exceeded, creating waves in the early stages of the filling process. This phenomenon was due to small differences in the velocities at the gates. These differences were in turn imposed by the metallostatic pressure of the sprue.

The waves did not cease until the sprue was saturated with liquid metal. From that moment on, the metallostatic pressure acted uniformly on each gate. The waves disappeared to give way to a progressive filling as shown in Figure 7a. In addition, the velocity in the gates area remained stable throughout the filling process, providing moderate turbulence that minimized the risk of gas entrainment. Finally, the filling time was 5.2 s.

The behaviour of the liquid flow for the vacuum-assisted mould was more stable and homogeneous (Figure 7b). In the early stages of the filling process, the liquid entered the mould cavity at a high velocity; this was due to the vertical pouring configuration of the mould. The initial jet impact generated a turbulence, which was absorbed by the overflow. A slight wave effect was produced, but this effect was mitigated by the suction forces applied by the vacuum. Subsequently, a uniform filling process was obtained. The filling time in this case was 1.9 s.

The vacuum-assisted technique showed a more controlled filling, avoiding the possible defects of gas entrapment, inclusions or oxides.

The velocity profile of the gate cross-section during the filling process was obtained using the simulation software. Figure 8 shows the different velocities at the gates during the filling process. This velocity was divided in two stages: (i) up to 15% of filling (the metallic liquid was not stabilized because the gate has not been saturated) and (ii) up to 100% of moulds filling (the metal liquid was stabilized at the gate).

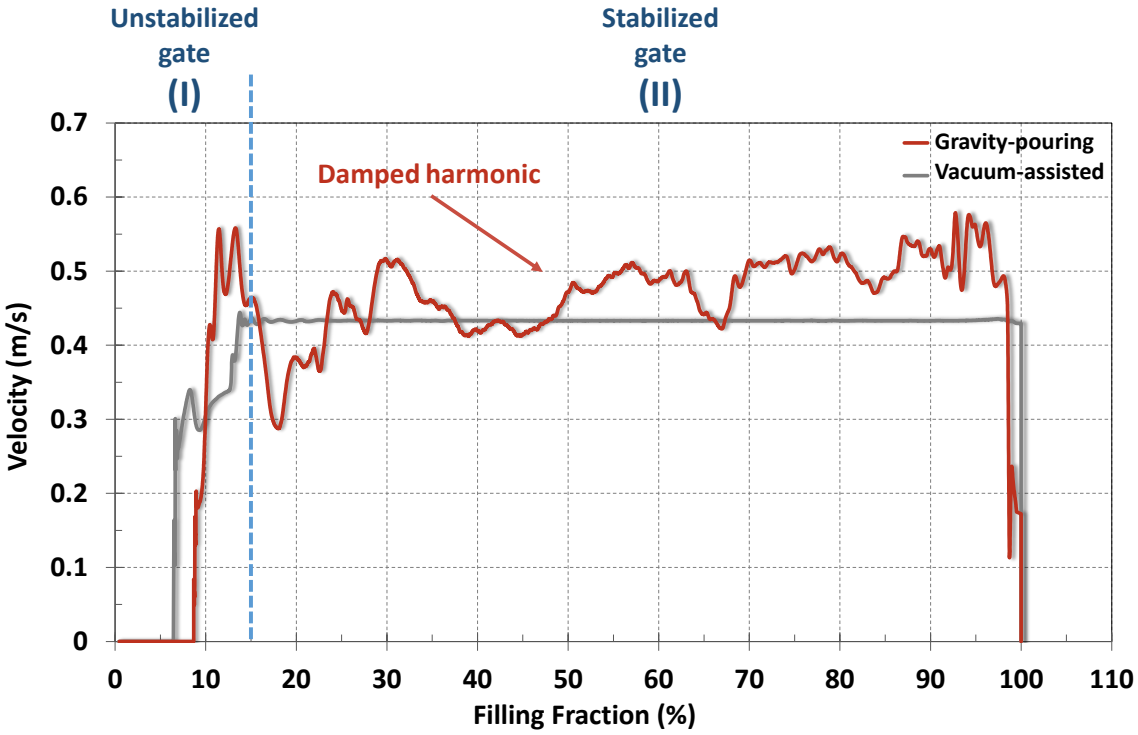

Figure 8. Velocity profile on the gates of both moulds during the filling process.

For the gravity-pouring mould, in stage (i), a strong increase in velocity was observed, which descended rapidly, with the highest value being 0.56 m/s. The velocity fluctuations generated the waves previously described.

In contrast, the vacuum-assisted technique presented two phases within the first stage. In the first phase, a sudden increase in velocity was observed. The liquid entrance was placed at the top of the mould; therefore, the gravity force acted in favour of the filling. In the second phase, the filling cup was saturated with liquid metal and the velocity gradually increased to the optimum filling velocity.

Stage (ii) represents the filling process when the metal liquid was stabilized at the gate. As shown in Figure 8, the gravity-pouring mould showed a filling with fluctuations over an average value of 0.48 m/s. The initial source effect dragged these fluctuations during the filling process. In addition, a damped harmonic state was observed in which the flow-generated waves decreased in amplitude as the filling process was completed. This is consistent with Figure 7a, where waves generated by the source effect tended to decrease and the flow became more stable. High runner pressures and large areas in the cavity result in higher gate velocities [49,50]. Even so, only in specific cases did the average velocity exceed the critical value of 0.5 m/s. Therefore, there was low risk of gas entrapment.

For the stage (ii) in the vacuum-assisted technique, a constant gate velocity of 0.43 m/s was observed. The filling velocity only depends on the gravity force, the vacuum force and the gate area. These three parameters were constant during the process and therefore the velocity was constant in this second filling stage.

3.2. Result of Solidification

Figure 9 shows the temperature distribution measured in both moulds and the exponential regression of the cooling rates. For the gravity-pouring mould, the temperature increased to a maximum of 389 ± 5 °C. The curve of the temperature had a large amplitude, due to the volume/area ratio of the part. The thermal energy had to be evacuated through the walls of the mould. When the mould heated up, the temperature difference between the casting surface and the mould became smaller and smaller, so the thermal evacuation decreased. The average cooling rate was −2.56 °C/s. The exponential regression shows a R^2 = 0.96 and an exponent of 0.00023.

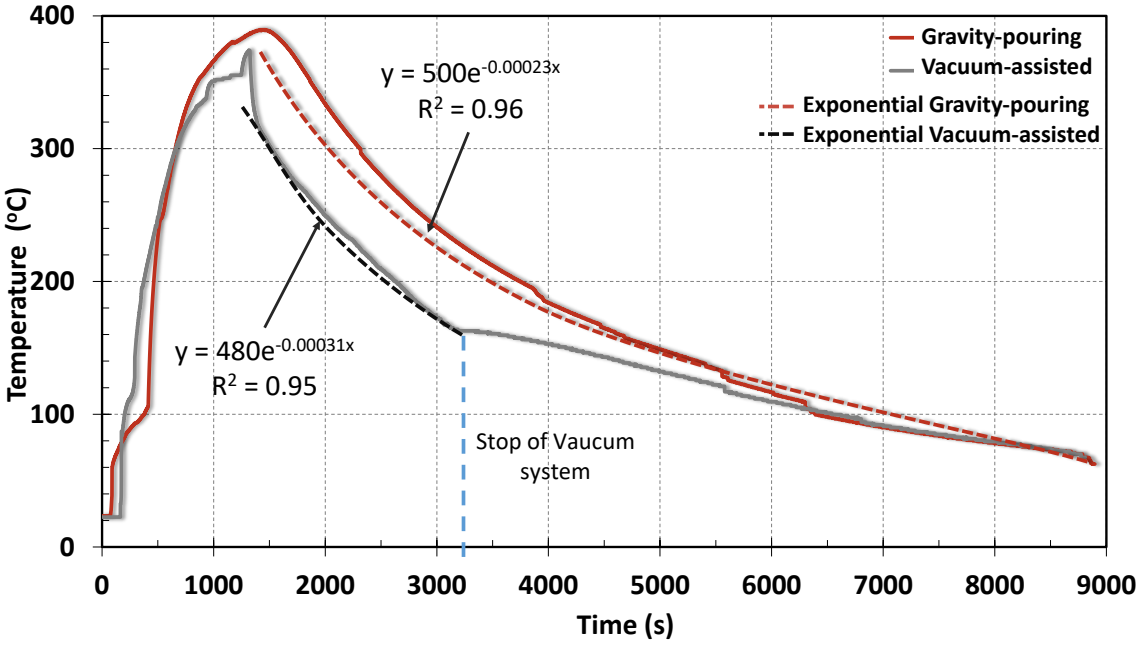

Figure 9. Temperature profile measured on the moulds after filling.

On the other hand, the temperature of the vacuum-assisted mould reached 374 ± 5 °C. As can be seen in Figure 9, the cooling distribution can be divided in two phases, before and after 3100 s. After this point, the vacuum system was turned off. The vacuum only has an effect during the solidification process; once the part is solidified, the vacuum system does not apply. The cooling rate was −9.08 °C/s. The exponential regression shows a R^2 = 0.95 and an exponent of 0.0003.

As can be seen in Figure 9, the exponent of the equation was higher in the vacuum-assisted mould, therefore the vacuum-assisted cooling was quicker than for the gravity-pouring mould. The higher thermal dissipation was due to the vacuum suction, as it removed the hot gases that were generated during the casting process, evacuating a higher heat flow. In addition, the proximity of the hot runner in the gravity-pouring casting could prevent the heat evacuation. Therefore, the turning point on the curve and the subsequent cooling process in the vacuum-assisted mould occurred earlier.

The thermal behaviour of both moulds was quite similar, as both moulds were built with the same 3DP technique, the same material and the same wall thickness. In addition, it can be observed that the total time cycle was very similar for both moulds, concluding that the application of vacuum did not excessively affect the solidification process. Despite that, the vacuum considerably improved the homogeneity in the filling, extracting most of the gases formed during the casting process, which is advantageous for reducing porosity.

3.3. Roughness

The principal parameters that influence the surface roughness of castings are (i) the mould material: type, morphology, size and grain distribution, (ii) the mould manufacturing process: compaction and

layer height, (iii) the pouring of the aluminium alloy: pouring temperature, (iv) the vacuum applied: degree of vacuum imposed.

All parameters were kept constant in this research, except the degree of vacuum applied during filling (no vacuum for the gravity-pouring mould and 150 ± 1 mbar in absolute pressure for the vacuum-assisted mould).

As shown in Figure 10a, the roughness in the gravity-pouring part showed a considerable dispersion of values in all zones and directions. The roughness in Zone I in both directions was a little more stable than in the rest. This was due to the higher metallostatic pressure in the lower area of the part (Zone I), favouring a more accurate reproduction of the mould surface. For the upper zones of the part, the metallostatic pressure was lower and therefore the values of the measurements were more dispersed.

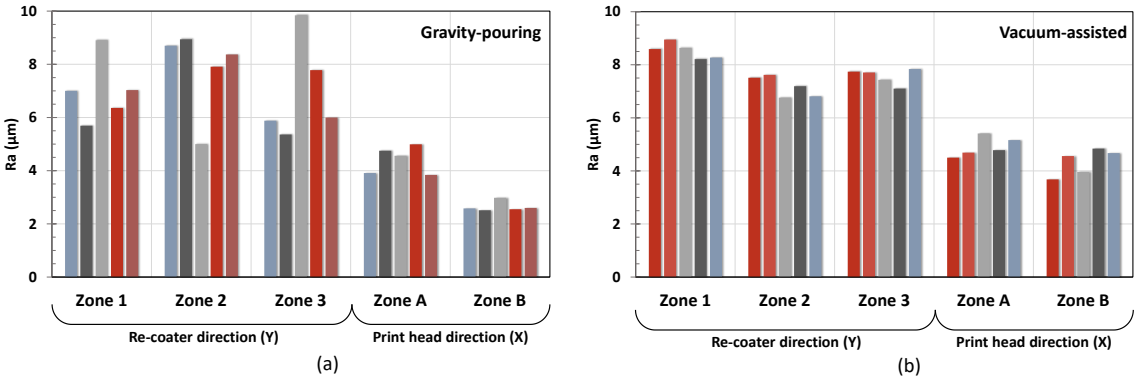

Figure 10. (**a**) Roughness distribution for the gravity-pouring part. (**b**) Roughness distribution for the vacuum-assisted part.

The roughness values for the vacuum-assisted part, Figure 10b, were a little higher than for the gravity-pouring, but significantly more uniform in all zones and directions. This was because the vacuum pressure created a suction effect that attracted the molten metal against the walls of the mould, helping the liquid metal to penetrate more into the capillaries formed between the calcium sulphate particles.

The gravity-pouring part had an average value of Ra = 3.52 µm in the direction of the printing-head movement (X direction) and Ra = 7.02 µm in the re-coater direction (Y direction). The average roughness values of the vacuum-assisted part were Ra = 4.63 µm in the X direction and Ra = 7.76 µm in the Y direction.

The overall roughness values could be reduced if the machine could compact the powder during the manufacturing process [51]. The results obtained in the normal direction to the layer construction (re-coater direction) can be reduced by using a lower layer height. Creating a thinner layer would reduce the roughness of the mould, but increase the printing time. Another option could be to apply an infiltration post-process to the moulds to increase the surface quality. However, the values obtained are tolerable compared to traditional sand casting (10 µm < Ra < 25 µm) [52].

3.4. Dimensional Quality

One of the most critical parameters for metal casting is dimensional accuracy. The moulds showed dimensional and geometrical deviations due to two factors. Firstly, the bleeding effect, caused by capillary action, which attracts the liquid binder to the adjacent calcium sulphate particles. This effect caused deformations in each two-dimensional layer, affecting the final dimensions of the moulds [28]. Secondly, the heat treatment applied to the moulds caused a variation in the bonding bridges among the particles, resulting in volumetric shrinkage in the mould cavity.

As shown in Figure 11, step 1 reflects the comparison between the as-built mould cavity and the nominal CAD. The gravity-pouring mould showed a low standard deviation (0.087 mm). The measured

values indicated results very close to the nominal (0 value). For the upper points (55.52%) the average value did not exceed 0.07 mm. The lower points (44.48%) also had an average value of −0.07 mm. On the other hand, vacuum-assisted mould showed an even smaller standard deviation (0.054 mm). Moreover, the average values are even closer to the nominal values, 0.04 mm for the upper (46%) and lower (54%) points, respectively. Therefore, both moulds have a similar accuracy, with a standard deviation around ±0.05 mm, which indicates that the AM machine has a good geometrical accuracy and high repeatability during the manufacturing process.

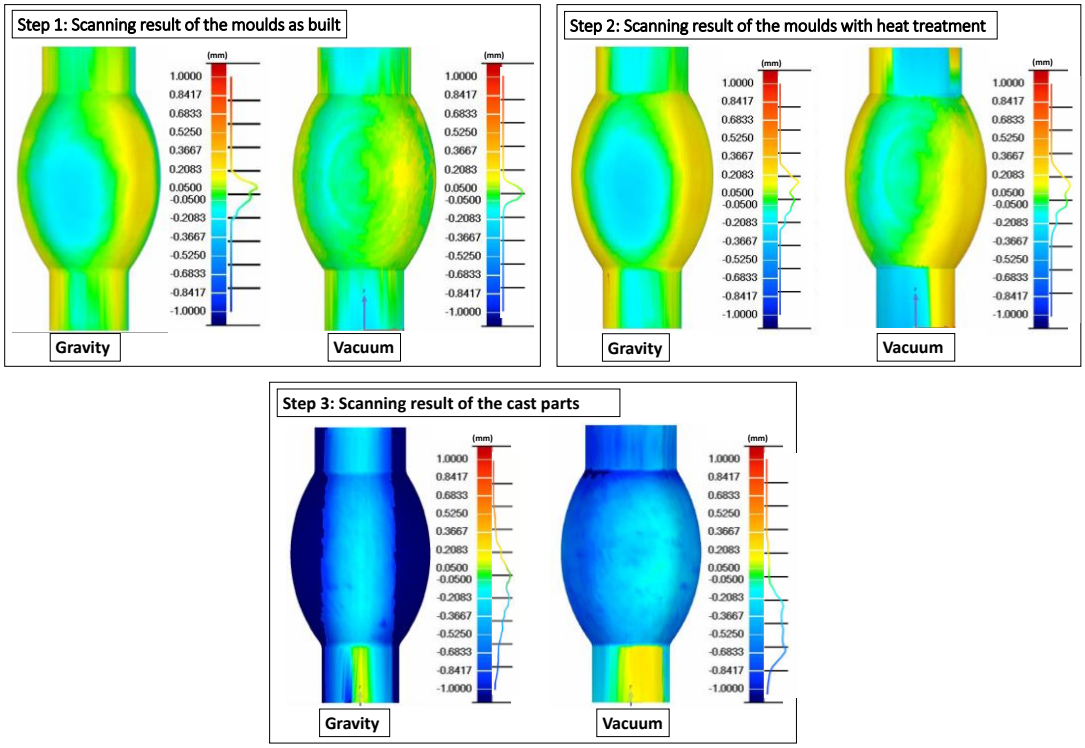

Figure 11. Scanning the three steps of the casting process for both techniques.

Step 2 shows the comparison between the mould cavity after heat treatment and the nominal CAD. The average value for the gravity-pouring mould became 0.13 mm and −0.09 mm in the upper and lower deviation, respectively (Table 4). The number of positive points also increased from 44.48% to 62.95%. In the case of the vacuum-assisted mould, the values in the upper and lower deviation were 0.13 and −0.10, respectively. In addition, the number of positive points was redistributed to 65.31%.

Table 4. Results of dimensions quality for moulds and parts obtained by casting.

		As-Built		After Heat-Treatment		Casting	
	Measure	**Gravity**	**Vacuum**	**Gravity**	**Vacuum**	**Gravity**	**Vacuum**
Upper deviation	Points (%)	55.52	46.00	62.95	65.31	28.67	4.28
	Average (mm)	0.07	0.04	0.13	0.13	0.17	0.14
Lower deviation	Points (%)	44.48	54.00	37.05	34.59	71.83	92.69
	Average (mm)	−0.07	−0.04	−0.09	−0.10	−0.37	−0.44
Standard deviation (mm)		0.087	0.054	0.129	0.133	0.352	0.253

The heat treatment for both moulds increase in the standard deviation (Table 3) and average values for both moulds indicates a higher dispersion in the points and, therefore, an increase in the geometric error before the pouring process. The volume reduction was also reflected through the

increase in the percentage of positive points. This meant that the castings had smaller dimensions than the nominal CAD. Therefore, the heat treatment added a geometric error and caused a reduction in the volume of the cavity in both moulds.

Finally, step 3 shows the comparison of the part and the nominal CAD. For the casting part, the positive values represent the negative values of the mould. Therefore, in the gravity-pouring part, the positive points decreased to 28.67% with an average value of 0.17 mm. Consequently, 71.83% of the points are in negative values, with an average of −0.37 mm. In addition, the standard deviation for the casting part achieved the highest value in all of the complete process, with a result of 0.35 mm. However, the vacuum-assisted part presented less geometric defects than the gravity-pouring alternative.

As shown in Table 4, the standard deviation was 0.25 mm and 92.69% of the points were at 0.44 mm.

The vacuum-assisted was able to improve the geometric quality of the final part, since the error was similar to the sum of the aluminium shrinkage (linear thermal shrinkage for this aluminium alloy is 1.2%, which for this geometry is −0.3 mm) plus the geometric error of the heat-treated mould.

3.5. Porosity

Porosity of castings directly affects the mechanical properties of the castings. Large pores reduce the loading area and more easily induce crack propagation.

To evaluate the volumetric porosity of the parts, it was necessary to calculate the bulk density of the parts using the following expression [38]:

$$\rho_p = \frac{m_1}{m_1 - m_2} \times \rho_w \tag{1}$$

where: ρ_p and ρ_w are the specimen density and water density, respectively; m_1 and m_2 are the mass of the specimen in air and water, respectively. Finally, the following expression was used to calculate the volumetric porosity:

$$P = \left(1 - \frac{\rho_p}{\rho_r}\right) \times 100\% \tag{2}$$

where: ρ_r is the actual density of aluminium ENAB46000 (2760 kg/m^3) according to EN1706 [53]. Table 5 shows the volumetric porosity results for the different part zones in both techniques.

Table 5. Volumetric porosity in the different zones of the parts.

Place	Gravity-Pouring (P)	Vacuum-Assisted (P)
Zone I	1.623 ± 0.019%	1.579 ± 0.017%
Zone II	2.295 ± 0.011%	1.773 ± 0.021%
Zone III	8.171 ± 0.016%	2.100 ± 0.014%
Average	4.029 ± 0.015%	1.817 ± 0.017%

Volumetric porosity increased with the zone. This was due to the vertical filling in both moulds. The density of the bubbles entrapped was lower than the metallic liquid, so the bubbles ascended and accumulated in the upper part of the casting. The vacuum pressure reduced the porosity of the parts in each zone, resulting in an average porosity 2.212% lower than in the gravity-pouring part.

To analyse porosity in depth, a study of the number, size and shape of the pores was carried out. Figure 12 shows the statistical distribution of the pores according to their size for each zone and location. Pore size was evaluated using Feret's maximum diameter.

The following can be deduced: (i) the pore size is in general between 10 and 14 µm for the gravity-pouring casting and between 0 and 14 µm for the vacuum-assisted casting. Therefore, the vacuum pressure decreases the pore size. (ii) The number of pores diminished in all areas with the vacuum-assisted casting. (iii) For both parts, the number of pores increased in Zones II and III,

as explained in the previous paragraph. On the other hand, Figure 12 reveals that the number of pores increased on the outside of the parts regardless of the zone. The reason is that the gas entrapped by the metal liquid could not be evacuated before solidification. Preheating of the mould is recommended to avoid this phenomenon.

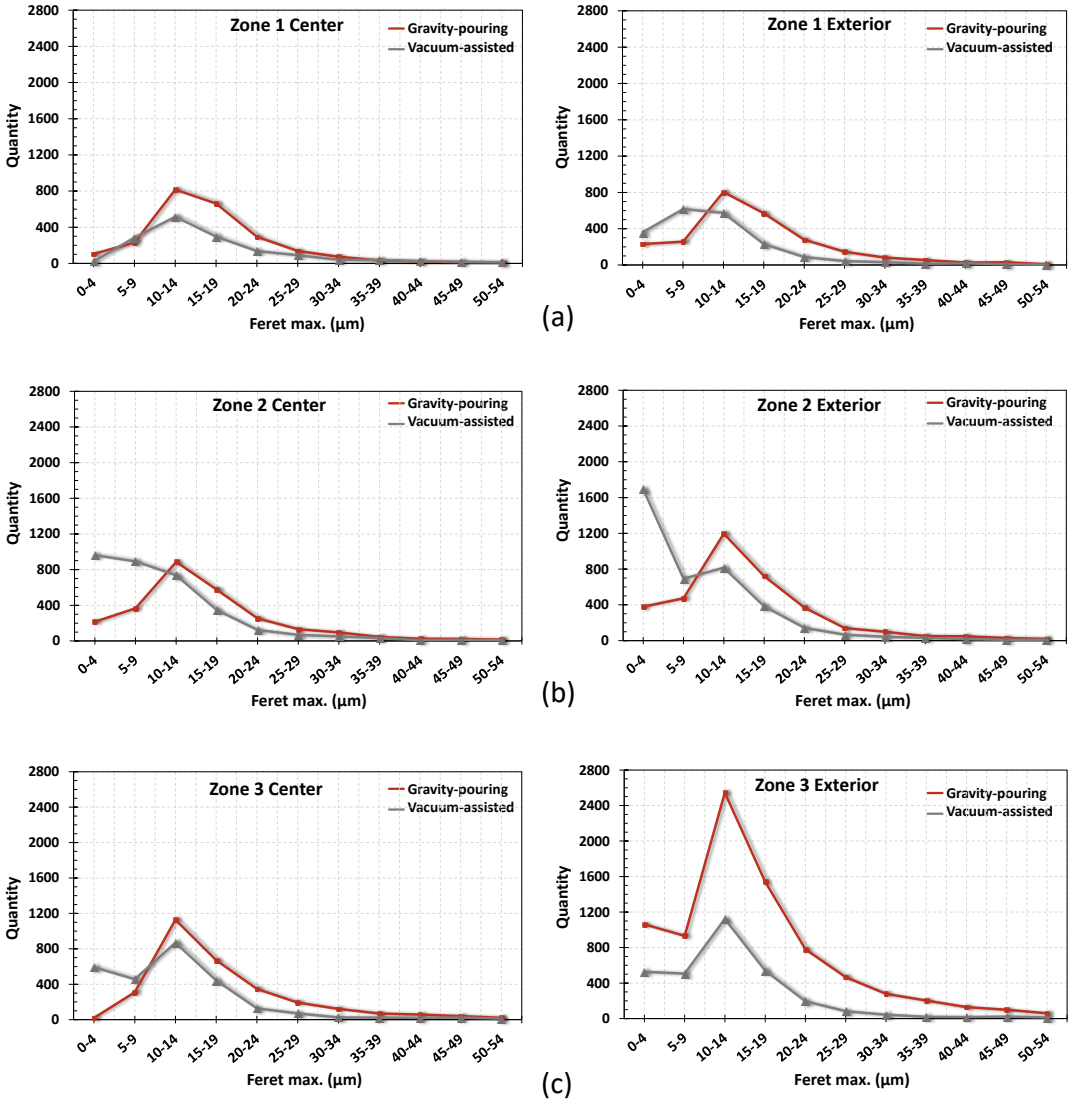

Figure 12. Statistical analysis of pore size by area and location. (**a**) Zone I, (**b**) zone II and (**c**) zone III.

Figure 13 shows the pores' morphology. Circularity of pores was calculated according to the following expression:

$$C = 4\pi \frac{a}{p^2} \tag{3}$$

where: C is the circularity of the pore; a is the area occupied by the pore and p is the perimeter of the pore.

Circularity in the vacuum-assisted part increased in all zones and locations. Therefore, it can be stated that when the size of the pores decreases, the circularity increases. In contrast, the larger pores had more irregular shapes, due to the defects associated with contraction by solidification, among others. The circularity of these particles was very low. Finally, the trend in morphology is very similar in all the analysed samples. For the gravity-pouring part, the circularity is grouped around 0.3; this indicates sharper and more irregular pores. However, for the vacuum-assisted part, the circularity tends to be higher (0.6), indicating more rounded pores.

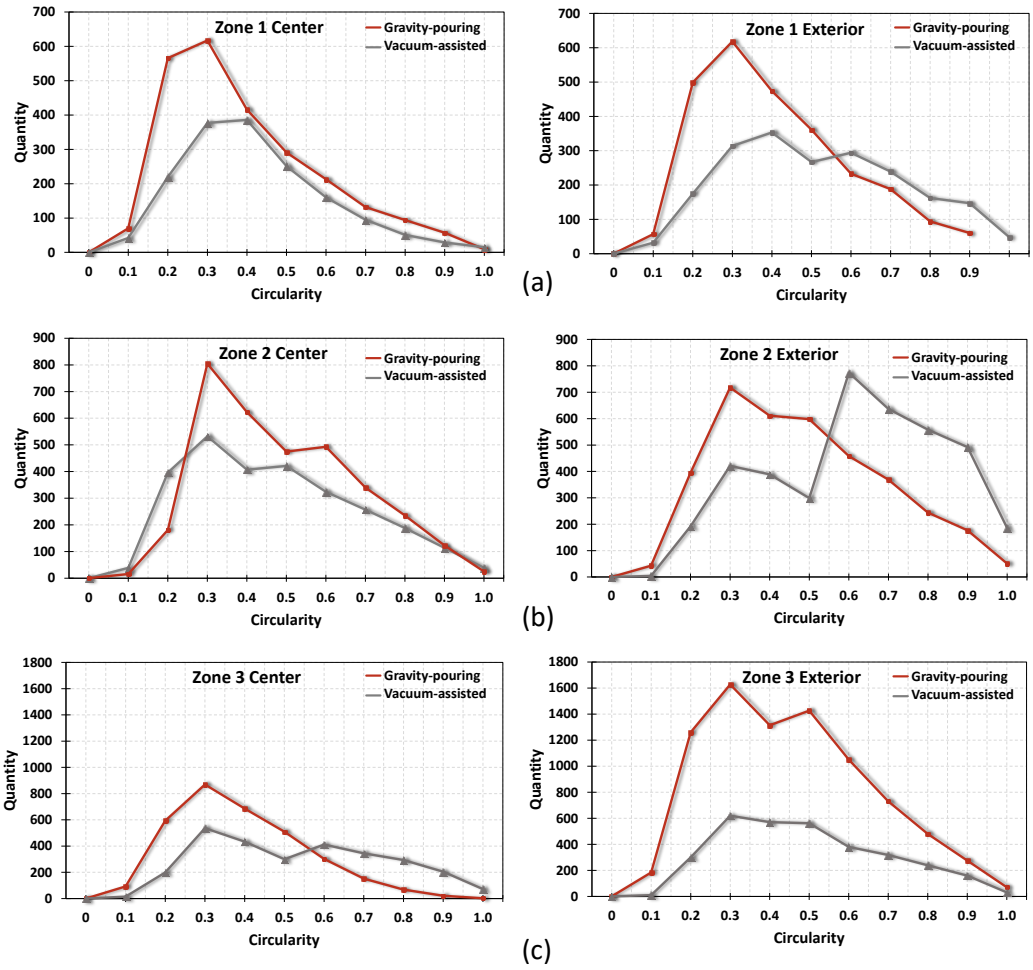

Figure 13. Statistical data on pore circularity for each area and location. (**a**) Zone I, (**b**) zone II and (**c**) zone III.

Figure 14 shows the morphology of pores in every zone in the parts: (i) Pores with sharp corners associated with shrinkage (Figure 14a); (ii) Oval-shaped pores with less sharp corners, resulting from a combination of shrinkage and gas entrapment (Figure 14b) and (iii) rounded-shaped pores associated with gas entrapment (Figure 14c). These three types of pores appeared in all specimens [24,34,38].

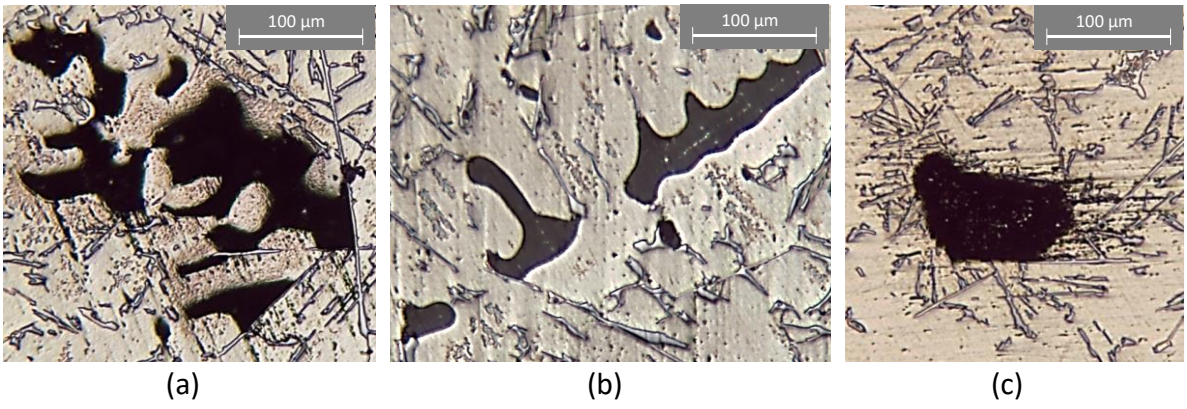

Figure 14. Different types of pores found in all samples. (**a**) Pores associated with shrinkage, (**b**) pores associated with shrinkage and gas entrapment and (**c**) pores associated with gas entrapment.

Table 6 shows the summary of the porosity results for each technique, zone and location of specimens. The application of vacuum results in a significant reduction in the average pore size (47.3%). Meanwhile, the maximum diameter, the minimum diameter and the number of pores also decrease with the application of vacuum.

Table 6. Summary of porosity for both techniques.

Zones	Location	Technique	Quantities of Pores	Avg. Size (μm)	Big Porous (>55 μm)	Max. Diameter (μm)	Min. Diameter (μm)
Zone I	Centre	Gra.	2465	19.39	73	750.64	2.00
		Vac.	1624	9.26	28	501.35	0.26
	Exterior	Gra.	2601	21.21	116	667.31	1.85
		Vac.	2031	12.16	67	462.14	0.64
Zone II	Centre	Gra.	2717	19.53	85	802.15	1.93
		Vac.	3316	12.06	43	418.24	0.72
	Exterior	Gra.	3664	20.80	139	1591.29	1.90
		Vac.	3951	10.81	38	647.66	1.05
Zone III	Centre	Gra.	3294	36.89	211	1667.02	3.01
		Vac.	2808	18.08	48	658.11	1.11
	Exterior	Gra.	8413	19.20	272	1125.53	1.85
		[M1] Vac.	3188	14.79	56	618.82	0.93

Large pores (>55 μm) have very irregular shapes and a random distribution. The number of large pores decreased up to 78% for the vacuum-assisted part, demonstrating that the application of vacuum pressure significantly reduces the size of the large pores. However, it was not sufficient to eliminate small pores (<55 μm).

The combination of volumetric porosity and average pore size results shows that the gravity-poured part (4.03% and 22.82 μm) is significantly larger than the vacuum assisted part (1.82% and 12.85 μm).

A high degree of vacuum during the casting is beneficial for reducing the entrapment of gases in the molten metal. Therefore, the choice of the correct value can significantly reduce the gas porosity and improve the mechanical properties of the casting part.

4. Conclusions

This paper presents the first research in which vacuum is applied to casting moulds manufactured by 3D printing. Furthermore, the study shows the feasibility of using vacuum suction with moulds manufactured by the Binder Jetting AM technique, concluding:

1. Simulation software made it possible to understand the behaviour of the metal flow inside the moulds. Simulation results permitted the optimization of the geometries of the filling system to avoid errors and improve the cooling of parts.
2. Roughness in the gravity-pouring part shows a significant dispersion in all zones of the part. However, the average values of roughness for the vacuum-assisted part are more uniform. Therefore, the use of vacuum leads to a part with a very homogeneous surface and higher quality.
3. The AM machine introduces a small error during manufacturing (bleeding effect). On the other hand, the error induced by the heat treatment in the moulds is very similar. However, the vacuum-assisted technique provides very good geometrical quality to the final part, reducing defects found when using the gravity-pouring technique.
4. The vacuum-assisted technique reduces volumetric porosity by 2.21%. In addition, the average pore size, the number of total pores and the number of large pores were significantly less. On the other hand, applying the vacuum technique increases the pore roundness, improving the mechanical properties of castings.

In future works, infiltration processes will be applied to increase the surface quality of moulds. In addition, the effect of mould preheating on the porosity of parts will be analysed.

Author Contributions: Conceptualization, P.R.-G., P.E.R.V., A.I.F.-A., M.A.C.-S., J.B.G.; methodology, P.R.-G. and P.E.R.V.; software, P.R.-G.; validation, P.R.-G.; formal analysis, P.R.-G.; investigation, P.R.-G. and P.E.R.V.; resources, P.R.-G., P.E.R.V., A.I.F.-A., M.A.C.-S., J.B.G.; writing—original draft preparation, P.R.-G. and P.E.R.V.; writing—review and editing, A.I.F.-A., M.A.C.-S., J.B.G.; supervision, J.B.G.; project administration, J.B.G.; funding acquisition, J.B.G. and A.I.F.-A. All authors have read and agreed to the published version of the manuscript.

Funding: The authors thank the Ministry of Science, Innovation and Universities of Spain for the support through the research project with reference DPI2017-89840-R.

Conflicts of Interest: The authors declare no conflict of interest.

References

1. Wohlers, T. *3D Printing and Additive Manufacturing State of the Industry: Annual Worldwide Progress Report*; Wohlers Associates: Fort Collins, CO, USA, 2018.
2. ISO/ASTM 52900:2015 Standard. *Additive Manufacturing General Principles—Terminology*; International Organization for Standardization: Geneva, Switzerland, 1996.
3. Derby, B. Additive manufacture of ceramics components by inkjet printing. *Engineering* **2015**, *1*, 113–123. [CrossRef]
4. Bassoli, E.; Atzeni, E. Direct metal rapid casting: Mechanical optimization and tolerance calculation. *Rapid Prototyp. J.* **2009**, *15*, 238–243. [CrossRef]
5. Ayres, T.J.; Sama, S.R.; Joshi, S.B.; Manogharan, G.P. Influence of resin infiltrants on mechanical and thermal performance in plaster binder jetting additive manufacturing. *Addit. Manuf.* **2019**, *30*, 100885.
6. Lumley, R.N. Aluminium Investment Casting and Rapid Prototyping for Aerospace Applications. In *Fundamentals of Aluminium Metallurgy*, 1st ed.; Elsevier Ltd., Woodhead Publishing: Amsterdam, The Netherlands, 2019; pp. 123–158.
7. Butscher, A.; Bohner, M.; Roth, C.; Ernstberger, A.; Heuberger, R.; Doebelin, N.; Von Rohr, P.R.; Müller, R. Printability of calcium phosphate powders for three-dimensional printing of tissue engineering scaffolds. *Acta Biomater.* **2012**, *8*, 373–385. [CrossRef]
8. Farzadi, A.; Solati-Hashjin, M.; Asadi-Eydivand, M.; Osman, N.A.A. Effect of layer thickness and printing orientation on mechanical properties and dimensional accuracy of 3D printed porous samples for bone tissue engineering. *PLoS ONE* **2014**, *9*, e108252. [CrossRef]
9. Mostafaei, A.; Stevens, E.L.; Ference, J.J.; Schmidt, D.E.; Chmielus, M. Binder jetting of a complex-shaped metal partial denture framework. *Addit. Manuf.* **2018**, *21*, 63–68. [CrossRef]
10. Kang, J.; Ma, Q. The role and impact of 3D printing technologies in casting. *China Foundry* **2017**, *14*, 157–168. [CrossRef]
11. Chen, Z.; Li, Z.; Li, J.; Liu, C.; Lao, C.; Fu, Y.; Liu, C.; Li, Y.; Wang, P.; He, Y. 3D printing of ceramics: A review. *J. Eur. Ceram. Soc.* **2019**, *39*, 661–687. [CrossRef]
12. Upadhyay, M.; Sivarupan, T.; El Mansori, M. 3D printing for rapid sand casting—A review. *J. Manuf. Process.* **2017**, *29*, 211–220. [CrossRef]
13. Bassoli, E.; Gatto, A.; Iuliano, L.; Violante, M.G. 3D printing technique applied to rapid casting. *Rapid Prototyp. J.* **2007**, *3*, 148–155. [CrossRef]
14. Huang, Y.; Leu, M.C.; Mazumder, J.; Donmez, A. Additive manufacturing: Current state, future potential, gaps and needs, and recommendations. *J. Manuf. Sci. Eng. Trans. ASME* **2015**, *137*, 1–11. [CrossRef]
15. Almaghariz, E.S.; Conner, B.; Lenner, L.; Gullapalli, R.; Manogharan, G.P.; Lamoncha, B.; Fang, M. Quantifying the role of part design complexity in using 3D sand printing for molds and cores. *Int. J. Met.* **2016**, *10*, 240–252. [CrossRef]
16. Shangguan, H.; Kang, J.; Deng, C.; Hu, Y.; Huang, T. 3D-printed shell-truss sand mold for aluminum castings. *J. Mater. Process. Technol.* **2017**, *250*, 247–253. [CrossRef]
17. Kang, J.; Shangguan, H.; Deng, C.; Hu, Y.; Yi, J.; Wang, X.; Zhang, X.; Huang, T. Additive manufacturing-driven mold design for castings. *Addit. Manuf.* **2018**, *22*, 472–478. [CrossRef]
18. Deng, C.; Kang, J.; Shangguan, H.; Hu, Y.; Huang, T.; Liu, Z. Effects of hollow structures in sand mold manufactured using 3D printing technology. *J. Mater. Process. Technol.* **2018**, *255*, 516–523. [CrossRef]

19. Sama, S.R.; Wang, J.; Manogharan, G. Non-conventional mold design for metal casting using 3D sand-printing. *J. Manuf. Process.* **2018**, *34*, 765–775. [CrossRef]
20. Sama, S.R.; Badamo, T.; Lynch, P.; Manogharan, G. Novel sprue designs in metal casting via 3D sand-printing. *Addit. Manuf.* **2019**, *25*, 563–578. [CrossRef]
21. Wang, J.; Sama, S.R.; Manogharan, G. Re-thinking design methodology for castings: 3D sand-printing and topology optimization. *Int. J. Met.* **2019**, *13*, 2–17. [CrossRef]
22. Yang, L.; Chai, L.H.; Liang, Y.F.; Zhang, Y.W.; Bao, C.L.; Liu, S.B.; Lin, J.P. Numerical simulation and experimental verification of gravity and centrifugal investment casting low pressure turbine blades for high Nb-TiAl alloy. *Intermetallics* **2015**, *66*, 149–155. [CrossRef]
23. Behera, M.M.; Pattnaik, S.; Sutar, M.K. Thermo-mechanical analysis of investment casting ceramic shell: A case study. Meas. *J. Int. Meas. Confed.* **2019**, *147*, 106805. [CrossRef]
24. Sun, J.; Le, Q.; Fu, L.; Bai, J.; Tretter, J.; Herbold, K.; Huo, H. Gas entrainment behavior of aluminum alloy engine crankcases during the low-pressure-die-casting process. *J. Mater. Process. Technol.* **2019**, *266*, 274–282. [CrossRef]
25. Zhao, S.; Zhang, N.; Zhou, X.; Zhang, L. Particle shape effects on fabric of granular random packing. *Powder Technol.* **2017**, *310*, 175–186. [CrossRef]
26. Du, W.; Ren, X.; Chen, Y.; Ma, C.; Radovic, M.; Pei, Z. Model guided mixing of ceramic powders with graded particle sizes in binder jetting additive manufacturing. In Proceedings of the ASME 2018 13th International Manufacturing Science and engineering Conference (MSEC 2018), College Station, TX, USA, 18–22 June 2018; pp. 1–9.
27. Ziaee, M.; Crane, N.B. Binder jetting: A review of process, materials, and methods. *Addit. Manuf.* **2019**, *28*, 781–801. [CrossRef]
28. Hodder, K.J.; Chalaturnyk, R.J. Bridging additive manufacturing and sand casting: Utilizing foundry sand. *Addit. Manuf.* **2019**, *28*, 649–660. [CrossRef]
29. Trombetta, R.; Inzana, J.A.; Schwarz, E.M.; Kates, S.L.; Awad, H.A. 3D Printing of calcium phosphate ceramics for bone tissue engineering and drug delivery. *Ann. Biomed. Eng.* **2017**, *45*, 23–44. [CrossRef]
30. Kafara, M.; Kemnitzer, J.; Westermann, H.H.; Steinhilper, R. Influence of binder quantity on dimensional accuracy and resilience in 3D-printing. *Procedia Manuf.* **2018**, *21*, 638–646. [CrossRef]
31. Vlasea, M.; Toyserkani, E.; Pilliar, R. Effect of gray scale binder levels on additive manufacturing of porous scaffolds with heterogeneous properties. *Int. J. Appl. Ceram. Technol.* **2015**, *12*, 62–70. [CrossRef]
32. Snelling, D.A.; Williams, C.B.; Druschitz, A.P. Mechanical and material properties of castings produced via 3D printed molds. *Addit. Manuf.* **2019**, *27*, 199–207. [CrossRef]
33. Castro-Sastre, M.A.; Fernández-Abia, A.I.; Rodríguez-González, P.; Martínez-Pellitero, S.; Barreiro, J. Characterization of materials used in 3D-printing technology with different analysis techniques. *Ann. DAAAM Proc. Int. DAAAM Symp.* **2018**, *29*, 947–954.
34. Rodríguez-González, P.; Valero, P.E.R.; Fernández-Abia, A.I.; Castro-Sastre, M.Á.; García, J.B. Feasibility of calcium sulfate moulds made by inkjet 3D printing for rapid casting of aluminium alloys. *Metals* **2020**, *10*, 802. [CrossRef]
35. Szklarz, Z.; Krawiec, H.; Rogal, Ł. The effect of vacuum suction casting on the microstructure and corrosion behavior of aluminium alloy 2017. *Mater. Sci. Eng. B-ADV.* **2019**, *240*, 23–32. [CrossRef]
36. Liu, S.; Cao, F.; Yi, J.; Zhao, X.; Zeng, J.; Ning, Z.; Sun, J. Effect of depressurizing speed on mold filling behavior and entrainment of oxide film in vacuum suction casting of A356 alloy. *Trans. Nonferrous Met. Soc. China* **2016**, *26*, 3292–3298. [CrossRef]
37. Cao, H.; Sun, Q.; Pu, Q.; Wang, L.; Huang, M.; Luo, Z.; Che, J. Effect of vacuum degree and T6 treatment on the microstructure and mechanical properties of Al–Si–Cu alloy die castings. *Vacuum* **2020**, *172*, 109063. [CrossRef]
38. Cao, H.; Hao, M.; Shen, C.; Liang, P. The influence of different vacuum degree on the porosity and mechanical properties of aluminum die casting. *Vacuum* **2017**, *146*, 278–281. [CrossRef]
39. Sun, Z.; Hu, H.; Chen, X. Numerical optimization of gating system parameters for a magnesium alloy casting with multiple performance characteristics. *J. Mater. Process. Technol.* **2008**, *199*, 256–264. [CrossRef]
40. Campbell, J. *Complete Casting Handbook: Metal. Casting Processes, Metallurgy, Techniques and Design*, 2nd ed.; Butterworth-Heinemann: Amsterdam, The Netherlands, 2011.

41. Rahmanian, I.; Wang, Y. Thermal conductivity of gypsum at high temperatures a combined experimental and numerical approach. *Acta Polytech.* **2009**, *49*, 16–20.
42. Craft, S.T.; Isgor, B.; Hadjusophocleous, G.; Mehaffey, J.R. Predicting the thermal response of gypsum board subjected to a constant heat flux. *Fire Mater.* **2008**, *32*, 333–355. [CrossRef]
43. Thomas, G. Modelling thermal performance of gypsum plasterboard-lined light timber frame walls using SAFIR and TASEF. *Fire Mater.* **2010**, *34*, 385–406. [CrossRef]
44. Shakor, P.; Sanjayan, J.; Nazari, A.; Nejadi, S. Modified 3D printed powder to cement-based material and mechanical properties of cement scaffold used in 3D printing. *Constr. Build. Mater.* **2017**, *138*, 398–409. [CrossRef]
45. 3D Systems Projet 660Pro Home Page. Available online: https://es.3dsystems.com/3d-printers/projet-cjp-660pro (accessed on 26 June 2020).
46. Lee, Y.S.; Nandwana, P.; Zhang, W. Dynamic simulation of powder packing structure for powder bed additive manufacturing. *Int. J. Adv. Manuf. Technol.* **2018**, *96*, 1507–1520. [CrossRef]
47. ISO 4288:1996 Standard. *Geometrical Product Specifications (GPS)—Surface Texture: Profile Method—Rules and Procedures for the Assessment of Surface Texture*; International Organization for Standardization: Geneva, Switzerland, 1996.
48. *ASTM E3–01:2017-Preparation of Metallographic Specimens*; ASTM International: West Conshohocken, PA, USA, 2011.
49. Sanitas, A.; Bedel, M.; El Mansori, M. Experimental and numerical study of section restriction effects on filling behavior in low-pressure aluminum casting. *J. Mater. Process. Technol.* **2018**, *254*, 124–134. [CrossRef]
50. Majidi, S.H.; Griffin, J.; Beckermann, C. Simulation of air entrainment during mold filling: Comparison with water modeling experiments. *Metall. Mater. Trans. B* **2018**, *49*, 2599–2610. [CrossRef]
51. Cao, S.; Qiu, Y.; Wei, X.; Zhang, H. Experimental and theoretical investigation on ultra-thin powder layering in three dimensional printing (3DP) by a novel double-smoothing mechanism. *J. Mater. Process. Tech.* **2015**, *220*, 231–242. [CrossRef]
52. Kalpakjian, S.; Schmid, S. *Manufacturing Engineering & Technology*, 7th ed.; Pearson: Chicago, IL, USA, 2014.
53. UNE-EN 1706: 2011 Standard. *Aluminio y aleaciones de aluminio. Piezas moldeadas. Composición Química y Características Mecánicas*; Asociacion Española de Normalización e Inspaeccion (AENOR): Madrid, España, 2011.